Optical Generation of High Carrier Densities in 2D Semiconductor Hetero-Bilayers

Jue Wang,[1,*] Jenny Ardelean,[2,*] Yusong Bai,[1,*] Alexander Steinhoff,[3] Matthias Florian,[3] Frank Jahnke,[3] Xiaodong Xu,[4] Mackillo Kira,[5,†] James Hone,[2,†] X.-Y. Zhu[1,†]

[1] Department of Chemistry, Columbia University, New York, NY 10027, USA

[2] Department of Mechanical Engineering, Columbia University, New York, NY 10027, USA

[3] Institute for Theoretical Physics, University of Bremen, 28334 Bremen, Germany

[4] Department of Physics and Department of Materials Science and Engineering, University of Washington, Seattle, WA 98195, USA

[5] Department of Electrical Engineering & Computer Science and Department of Physics, University of Michigan, Ann Arbor, MI, USA

ABSTRACT: Controlling charge density in two-dimensional (2D) materials is a powerful approach for engineering new electronic phases and properties. Such control is traditionally realized by electrostatic gating. Here, we report an optical approach for generation of high carrier densities utilizing transition metal dichalcogenide hetero-bilayers, $WSe_2/MoSe_2$, with type-II band alignment. By tuning the optical excitation density above the Mott threshold, we realize the phase transition from interlayer excitons to charge-separated electron/hole plasmas, where photoexcited electrons and holes are localized to individual layers. Remarkably, high carrier densities up to $4x10^{14}$ cm^{-2} can be sustained under both pulsed and continuous wave excitation conditions. These findings open the door to optical control of electronic phases in 2D hetero-bilayers.

One-sentence summary: From interlayer excitons to electron/hole plasmas at two-dimensional semiconductor heterojunctions.

[*] These authors contributed equally.

[†] To whom correspondence should be addressed. xyzhu@columbia.edu (XYZ); jh2228@columbia.edu (JH); mackkira@umich.edu (MK).

INTRODUCTION

Two-dimensional (2D) transition metal dichalcogenides (TMDCs) are emerging platforms for exploring a broad range of electronic, optoelectronic, and quantum phenomena. These materials feature strong Coulombic interactions, making them ideal for studying highly correlated quantum phenomena as a function of charge-carrier density. Seminal demonstrations include among others, charge-density waves and superconductivity in $TiSe_2$ and MoS_2 by electrostatic gating [1–4]. These exciting demonstrations have been possible due to the high charge carrier densities (~10^{14} cm^{-2}) achievable with ionic liquid gating. Under bias, a capacitive electrical bilayer is formed between the charge carriers in the 2D material and counter ions in the liquid. Among the limitations of using a liquid as dielectric is that controlling charge carrier density requires gate switching near room temperature, but the appearance of interesting electronic phases occurs mostly upon cooling on hour time scales under the gate bias. Alternatively, in TMDC type-II hetero-bilayers, photo-excited electrons and holes separate on femtosecond time scales [5,6] to form oppositely charged monolayers. While these spatially separated electrons and holes form Coulomb bound interlayer excitons [7–10], the insulating exciton gas can be transformed to conducting charge-separated electron/hole plasmas if excitation density is increased to above the Mott threshold (n_{Mott}) [11,12], as illustrated schematically at the top of Fig. 1 for the $WSe_2/MoSe_2$ hetero-bilayer studied here. The Mott transition has been observed in optically excited monolayer and bilayer WS_2 [13], but the electron and hole plasma exist in the same material which remains charge neutral. In contrast, TMDC hetero-bilayers host spatially sepaparted electron/holes with long lifetimes [7–10,14]. Therefore, these systems offer a unique opportunity to control high carrier densities in individual 2D monolayers. In this case, the resulting e/h bilayer across the hetero-interface in the presence of photo-excitation, particularly under CW conditions, resembles the capacitive electric bilayer in an ionic gated 2D material. Here we use photoluminescence (PL) spectroscopy and time-resolved reflectance spectroscopy to demonstrate optically driven Mott transition from interlayer exciton to charge-separated electron/hole plasmas in the $WSe_2/MoSe_2$ hetero-bilayer. The experimental findings are supported by calculations from quantum theory. The achieved carrier density is as high as $4x10^{14}$ cm^{-2}, more than two orders of magnitude above the Mott density.

RESULTS

Experiments: Mott Transition from Interlayer Exciton to Charge Separated Plasmas

We use transfer stacking to form $WSe_2/MoSe_2$ hetero-bilayers encapsulated by hexagonal boron nitride (h-BN), with the two TMDC monolayers aligned within the light-cone [15] for radiative interlayer exciton emission (twist angle $\theta = 4\pm2^o$ from K/K or K/K' stacking), with a dark hetero-bilayer sample with $\theta = 13\pm2^o$ (from K/K or K/K' stacking) as control (see Supplemental Materials Fig. S1 for optical images, Figs. S2 and S3 for monolayer alignment). The WSe_2 and $MoSe_2$ monolayers are exfoliated from flux-grown single crystals, each with defect density $< 10^{11}$ cm^{-2}, two orders of magnitude lower than in commonly used commercial crystals [16]. This is critical for suppressing defect-mediated non-radiative recombination previously seen to dominate TMDC hetero-bilayers [6] and for sustaining high excitation density in the charge separated electron/hole plasmas. All measurements are carried out with the samples at 4 K in a liquid helium cryostat. The spectroscopic measurements include steady-state PL with continuous wave (CW) excitation ($h\nu$ = 2.33 eV), time-resolved (TR) PL with pulsed excitation ($h\nu$ = 2.33 eV, pulse width 150 fs), transient reflectance spectroscopies with pulsed excitation ($h\nu$ = 1.82 eV, pulse duration 150 fs) (see Fig. S4 for experimental setup). At both excitation photon energies, we calculate the absorptance (percentage of incident light absorbed, see Fig. S6) to be 8% at the low excitation density limit, based on the reported dielectric functions of WSe_2 and MoS_2 monolayers [17]. We carefully calibrate experimental electron/hole density, n_{eh}, by including saturation of absorptance from self-consistent Maxwell-semiconductor Bloch equation calculations (see Supplemental Materials, Fig. S8 and S9, Table S1). Under the experimental conditions employed here, we find the measurements completely reproducible, i.e., there is no sample damage due to laser excitation. However, damage to other heterobilayer samples have been observed for laser excitation exceeding the upper limit shown here.

Figure 1a shows CW PL spectra from the $WSe_2/MoSe_2$ hetero-bilayer with n_{eh} spanning over four orders of magnitude ($1.6\text{x}10^{10} - 3.2\text{x}10^{14}$ cm^{-2}), achieved by varying excitation power density from ρ = 0.5 W/cm^2 to $1.5\text{x}10^5$ W/cm^2. We quantitatively calibrate the equilibrium excitation density based on $n_{eh} = F \cdot \sigma \cdot \tau_0$, where F is the incident photon flux, σ is the absorptance, and τ_0 is the population decay time constant determined in TR-PL; both σ and τ_0 are numerical functions of n_{eh} (see below) determined systematically through our computations and measurements, respectively. A complete set of spectra with normalized peak intensities is shown

for the 1.31-1.41 eV region in Fig. 1b. Also shown in Fig. 1a are PL spectra of $MoSe_2$ (blue) and WSe_2 (green) monolayers. The former is characterized by the neutral exciton (X_M) and the trion

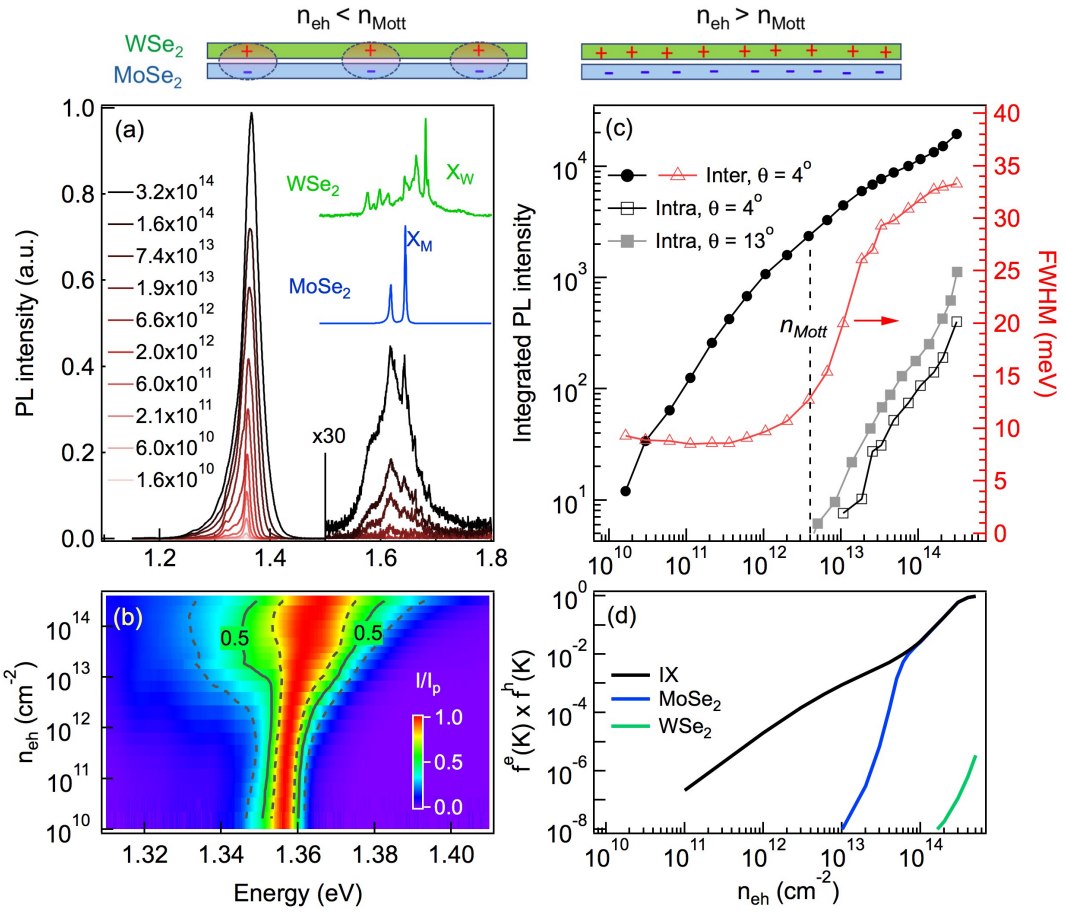

Fig. 1. Excitation density dependent photoluminescence (PL) and Mott transition in the $WSe_2/MoSe_2$ hetero-bilayer. PL spectra (a) and intensity normalized PL spectra (b) from a BN-encapsulated $WSe_2/MoSe_2$ hetero-bilayer with $\theta = 4\pm2^o$ angular alignment between the two monolayers. The spectra were obtained with CW excitation at $h\nu = 2.33$ eV and calibrated excitation densities (n_{eh}) between 1.6×10^{10} cm^{-2} and 3.2×10^{14} cm^{-2} at 4 K. The spectral region ($h\nu \geq 1.51$ eV) corresponding to PL emission from monolayer WSe_2 and $MoSe_2$ is multiplied by a factor of 30. Also in (a) are PL from monolayer WSe_2 (green) and monolayer $MoSe_2$ (blue). Shown on the 2D pseudo-color (normalized intensity, I/I_P, where I_P is peak intensity) plot in (b) are contours of 50% (solid curve) and 25% and 75% (dashed curves) of I_P. (c) Integrated intensities (left axis) of interlayer (1.2-1.5 eV, solid black circles) and intralayer (1.51-1.80 eV, open black squares) PL emission, as well as FWHM of the interlayer exciton peak (open red triangles, right axis), as a function of n_{eh}, as well as integrated intralayer PL intensities (solid grey squares) from a BN-encapsulated $WSe_2/MoSe_2$ hetero-bilayer with $\theta = 13\pm2^o$ angular alignment. (d) Computed joint electron-hole populations in the K valleys for interlayer exciton (black) and intralayer excitons in $MoSe_2$ (blue) and WSe_2 (green). The top of the figure is a cartoon illustrating the Mott transition in the $WSe_2/MoSe_2$ hetero-bilayer.

while the latter consists of a series of peaks assigned to exciton (X_W), trion, biexciton, etc., in agreement with previous reports [18–21]. At $n_{eh} \leq 1\text{x}10^{13}$ cm^{-2} in the hetero-bilayer, PL from intralayer excitons are completely quenched while interlayer exciton (IX) emission with E_{IX} = 1.3566±0.0005 eV (at $n_{eh} = 1.6\text{x}10^{10}$ cm^{-2}) dominates [7,22]. The IX peak grows with n_{eh} and blue-shifts only by ~8 meV in the entire excitation density range, as is known for coupled [23] and uncoupled [24] III-V quantum wells.

To experimentally detect the Mott transtion, we plot in Fig. 1c the n_{eh} dependences of the integrated intensities from interlayer PL (solid black circles) and its spectral full-width-at-half-maximum (FWHM, open red triangles) along with the intralayer PL (open black squares) integrated over the 1.5-1.75eV energy rage. The interlayer emission peak broadens significantly when the theory-assigned $n_{Mott} = 3\text{x}10^{12}$ cm^{-2} (vertical dashed line, see below) is crossed. The corresponding FWHM increases by as much as a factor of four, verifying that excitons (and the narrow linewidth they sustain) are absent above n_{Mott}. We also observe that intralayer PL, corresponding to broad emission from $MoSe_2$ and/or WSe_2 monolayer(s), reappears and grows for $n_{eh} > 1\text{x}10^{13}$ cm^{-2}. As the charge-separated e/h plasmas form at $n_{eh} > n_{Mott}$, the band offsets between the two TMDC monolayers are reduced due to both band-renormalization and charge separation. The latter can be understood from a simple capacitive model (see Supplemental Materials, page 11) which predicts from the e/h charge separation a voltage buildup, ΔV_C. This ΔV_C can cancel out the initial ~300 meV band offset [14], leading to the repopulation of the conduction (valence) band of WSe_2 ($MoSe_2$) and to intralayer radiative recombination. This interpretation is supported theoretically, Fig. 1d, which shows the computed source for PL emission, i.e. the probability of simultaneously finding electrons and holes in the K valleys of WSe_2 (green), $MoSe_2$ (blue), and between the two monolayers (black). The experimental onset of intralayer PL matches perfectly with the rise in the computed spontaneous emission source for $MoSe_2$, while PL from WSe_2 remains suppressed. Further support for this interpretation comes from PL measurement on the control sample of a $WSe_2/MoSe_2$ hetero-bilayer with $\theta = 13\pm2^o$ alignment. The large momentum mismatch between the K or $-K$ valleys across the interface means that the interlayer excitons are non-radiative [10]. Indeed, we observe no measurable IX emission, but only intralayer PL at $n_{eh} >> n_{Mott}$ (solid grey squares in Fig. 1c; see Fig. S10 for PL spectra).

We determine the lifetimes of interlayer exciton emission using TRPL under pulsed excitation ($h\nu$ = 2.33 eV; see Fig. S5 for instrument response function which gives time resolution of ~40

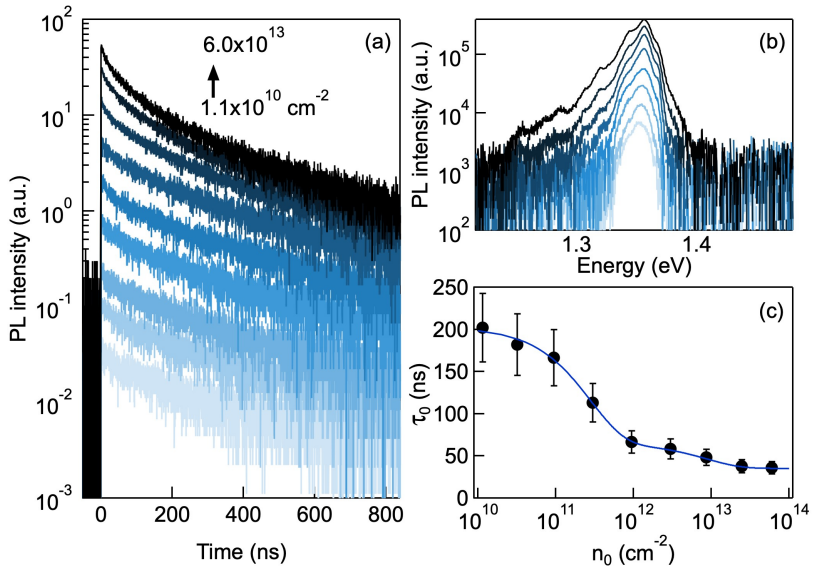

Fig. 2. **Time-resolved PL emission from interlayer excitons in the $WSe_2/MoSe_2$ hetero-bilayer.** The sample at 4 K is excited by pulsed laser (hν = 2.33 eV, pulse duration 150 fs). The energy-integrated emission from interlayer exciton (see spectra in panel b) is detected as a function of time, panel (a), for initial excitation densities of (from bottom to top) $n_0 = 1.1x10^{10}$, $3.0x10^{10}$, $9.4x10^{10}$, $3.0x10^{11}$, $9.4x10^{11}$, $3.0x10^{12}$, $8.7x10^{12}$, $2.5x10^{13}$, and $6.0x10^{13}$ cm^{-2}. (c) The initial decay time constants (solid circles) as a function of n_0. The solid line is biexponential fit to the data.

ps). Fig. 2a shows TRPL data in the broad initial excitation density range of $n_0 = 1.1x10^{10} – 6.0x10^{13}$ cm^{-2}. The corresponding time-integrated PL spectra, Fig. 2b, are similar to the CW PL spectra in Fig. 1a (see Fig. S11 for direct comparisons). The PL decays at low excitation densities ($10^{10\text{-}11}$ cm^{-2}) are close to single exponentials, with decay time constant of $\tau_0 = 200\pm40$ ns. As n_0 increases, particularly above n_{Mott}, the PL decay becomes faster and exhibits a major deviation from single exponential. This behavior is expected for plasma luminescence, as demonstrated in various III-V quantum well systems [25]. Above the Mott transition, luminescence from the e/h plasma scales approximately with n_{eh}^2. Additionally, carrier density may decay non-radiatively, e.g., via Auger recombination that scales approximately with n_{eh}^3. As a result, PL decays faster at higher carrier densities, but this is difficult to analyze quantitatively due to the varying Auger scattering cross section resulting from the expected density-dependent Coulomb screening. Fig. 2c plots the initial PL decay time constant as a function of n_0. Our PL lifetimes are one-two orders of magnitude longer than those of previous reports on $WSe_2/MoSe_2$ hetero-bilayers [7,22,26], suggesting the suppression of non-radiative recombination in the less defective TMDC samples used here.

These long PL lifetimes are essential to reaching excitation density well above the Mott threshold and to obtaining high equilibrium n_{eh} under CW excitation, as n_{eh} is proportional to τ_0.

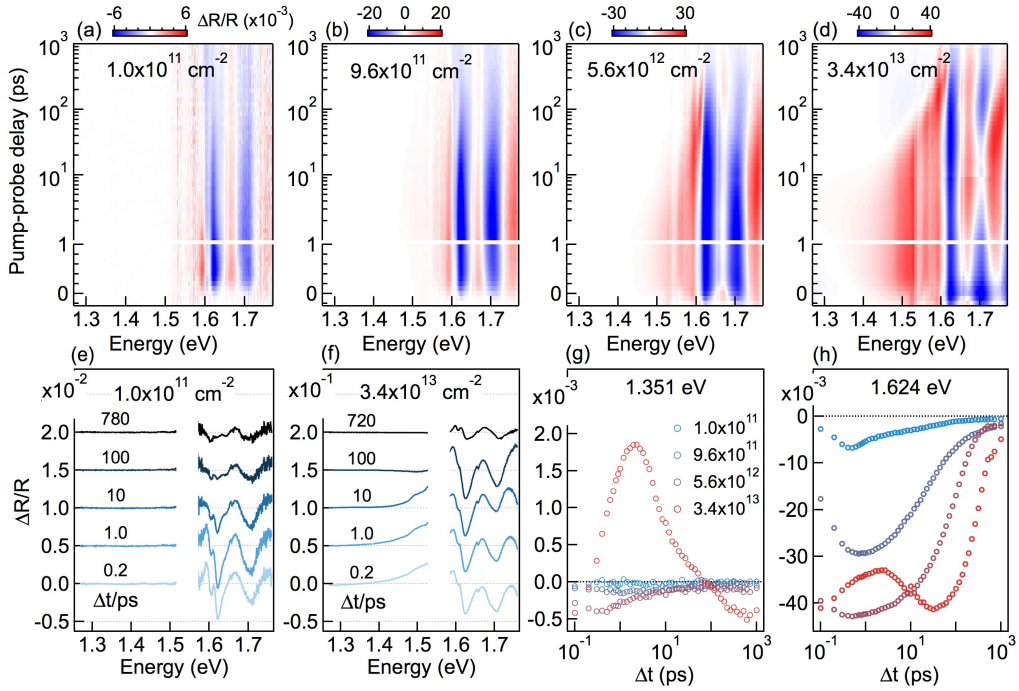

Fig. 3. Density dependent transient reflectance spectra from the $WSe_2/MoSe_2$ hetero-bilayer. The $WSe_2/MoSe_2$ hetero-bilayer was excited at hν = 1.82 eV with initial excitation densities of n_0 = (a) 1.0 x10^{11}, (b) 9.6x10^{11}, (c) 5.6x10^{12}, and (d) 3.4x10^{13} cm^{-2} at a sample temperature of 4 K. The excited sample is probed with white light and the pseudo-color scale is $\Delta R/R_0$ (blue = bleaching; red = induced-absorption). Transient reflectance spectra at selected pump-probe delays (Δt) at n_0 = (e) 1.0x10^{11} and (f) 3.4x10^{13} cm^{-2} are also shown. The probe regions around 1.55 eV are blocked out due to low intensity and noise from white light, which was generated by 1.55 eV laser light. Kinetic profiles obtained from vertical cuts at (g) 1.351 eV and (h) 1.624 eV in the 2D pseudo-color plots at the four n_0 values.

To further explore the properties of charge separated e/h plasmas in the $WSe_2/MoSe_2$ hetero-bilayer, we apply transient reflectance spectroscopy (time resolution ~40 fs, see Fig. S5) which has been used before to probe excitons and e-h plasma in TMDC monolayers [13] and charge separation in hetero-bilayers [5,6]. We excite the samples with a 150 fs pulse at 1.82 eV and probe the change in reflectance using broadband white light (1.2 – 1.8 eV). We present transient reflectance, $\Delta R/R_0$, as a function of pump-probe delay (Δt), where $\Delta R = R - R_0$; R is the reflectance at Δt and R_0 is the reflectance without the pump. At the 2D limit and low excitation densities, $\Delta R/R_0$ is proportional to transient absorption [27]. Figures 3a-d show pseudo-color plots of transient

reflectance spectra in a broad range of excitation densities. At $n_0 \leq n_{Mott}$, Fig. 3a or 3b, each spectrum is dominated by two prominent photo-bleaching peaks at ~1.62 eV and ~1.70 eV, attributed to reduction of oscillator strength [6] of transitions in monolayer WSe_2 and $MoSe_2$, respectively. The induced absorption signal (red) on the sides of the main bleaching peaks can be attributed to shifts in intralayer transition energies resulting from competing effects of screening/Pauli blocking of the Coulomb interaction and band renormalization. Note that, at $n_0 < n_{Mott}$, $\Delta R/R_0$ is negligible below 1.5 eV, including the IX region. This is expected as the oscillator strength of interlayer exciton is two orders of magnitude lower than those of intralayer excitons in each monolayer [28]. The absence of $\Delta R/R_0$ signal below 1.5 eV is evident in horizontal cuts at selected Δt values, shown for $n_0 = 1x10^{11}$ cm^{-2} in panel (e).

In agreement with the CW results in Fig. 1a, transient reflectance spectra under pulsed excitation reveal plasma formation above the Mott density. At $n_0 = 5.6x10^{12}$ or $3.4x10^{13}$ cm^{-2} (Figs. 3c and 3d), the spectra show, in addition to bleaching of intralayer exciton transitions, broad induced absorption extending to the low energy end (~1.3 eV) of the probe window. These broad features are evident in horizontal cuts (spectra) at short pump-probe delays, as shown for $n_0 = 3.4x10^{13}$ cm^{-2} in Fig. 3f. This broad absorption feature is optical signature of a 2D plasma, which consists of broad induced absorption (positive) extending to the renormalized band gap and gain (negative) just above the band gap [13,29].

While the spectroscopic measurements presented here were obtained at 4 K, we have also carried out PL measurements as functions of both excitation density and temperature up to 48 K (Fig. S12). The broadening of PL emission peak across the Mott density is similarly observed at temperatures > 4 K. However, the decrease in the excitonic emission intensity with temperature and the broadening due likely to exciton-phonon scattering make quantitative analysis of the Mott transition less reliable at higher temperatures. Note also that the current manuscript focuses on the transition from inter-layer excitons to charge separated e/h plasma in the $WSe_2/MoSe_2$ hetero-bilayer, the Mott transitions from intralayer exciton to e-h plasma have also been observed in transient reflectance spectra for individual WSe_2 or $MoSe_2$ monolayer (Fig. S13 and S14). In the latter case, the e-h plasma is not charge separated and is overall charge neutral, similar to the observation of Chernikov et al. on WS_2 monolayer and bilayers[13].

Theory: Optical responses of interlayer excitons and e/h plasmas

To calculate the optical properties of photoexcited transition metal dichalcogenide (TMDC) hetero-bilayers, we solve the semiconductor Bloch equations (SBE) [30,31] for the microscopic inter-band polarizations $\psi_k^{he}(t)$

$$i\hbar\frac{d}{dt}\psi_k^{he}(t) = \left(\varepsilon_{k,0}^{e} + \varepsilon_{k,0}^{h} + \Sigma_{k,SXCH}^{e} + \Sigma_{k,SXCH}^{h}\right)\psi_k^{he}(t) - \left(1 - f_k^e - f_k^h\right)\left(d_k^{eh}E(t) + \sum_{k'} W_{k,k'}^{eh}\psi_{k'}^{he}(t)\right) \quad (1),$$

with a weak external probe field E(t) incident perpendicular on the TMDC hetero-bilayer. The photoexcited electrons and holes generated by a strong pump field are described in quasi-equilibrium by Fermi distribution functions f_k^a. The linear susceptibility

$$\chi(\omega) = \sum_{k,eh}\psi_k^{he}(\omega)\, d_k^{eh}/E(\omega) \quad (2)$$

in the frequency domain is used in a second step to derive reflectance and absorptance spectra, as detailed below.

In the SBE, material properties enter via band structures ε_k^a, screened Coulomb matrix elements W_q and dipole matrix elements d_k. Band structure renormalizations due to photoexcited carriers are given by the screened-exchange-Coulomb-hole self-energy $\Sigma_{k,SXCH}^{a}$, while plasma screening is described by a dielectric function in the long-wavelength approximation via $W_{k,k'}^{ab} = \varepsilon_{k-k',pl}^{-1}V_{k,k'}^{ab}$ [31]. The band structure of the unexcited $MoSe_2$-WSe_2 heterolayer is modeled under an effective-mass approximation for the relevant conduction- and valence-band valleys as shown in Fig. S8. The energetic ordering of the bands is inspired by first-principle calculations [14], while we adjust the band edges to match our experimental reflectance spectra. We assume that the effective masses are approximately given by the masses of the respective monolayers as provided in ref. 32. For the Q- and Γ-valleys we average over both materials. The band edges and masses are collected in Table S1.

The Coulomb interaction between carriers located in different TMD layers is significantly weaker than intra-layer Coulomb interaction due to the spatial separation of carriers in growth direction. To account for this effect, we use model Coulomb matrix elements in a two-dimensional layer basis $|\alpha\rangle = \{|MoSe_2\rangle, |WSe_2\rangle\}$:

$$V_{k,k}^{ab} = \sum_{\alpha,\beta} \bar{c_\alpha^a}(k)\bar{c_\beta^b}(k')c_\beta^b(k)c_\alpha^a(k')V_{k-k'}^{\alpha\beta}, \quad (3)$$

where the contribution of a certain layer α to the band a is given by $|c_\alpha^a(k)|^2$. We assign layer contributions according to the first principle results in ref. 14 as given in Tab. S1. The matrix elements $V_q^{\alpha\beta}$ are modeled by a macroscopic dielectric function $\varepsilon_{q,b}^{-1,\alpha\beta}$ and a form factor $F_q^{\alpha\beta}$ according to

$$V_q^{\alpha\beta} = \frac{e^2}{2\varepsilon_0 q}\varepsilon_{q,b}^{-1,\alpha\beta}F_q^{\alpha\beta} \quad (4)$$

The dielectric function for each layer combination is obtained by solving Poisson's equation for the respective dielectric structure [33] as shown in Fig. S9. The dielectric constants of the TMD materials are computed as geometric mean of the values given in ref. 34, where also layer widths are provided. The dielectric constant of hBN is taken from ref. 35. The layer-substrate distance h_1=0.5 nm has been found to be an appropriate value in ref. 33, while we assume that the two TMD layers are slightly closer to each other using h_2=0.3 nm. The form factor accounts for the confinement of carriers inside the atomically thin layers via the confinement functions $\xi^\alpha(z)$:

$$F_q^{\alpha\beta} = \int dz \int dz' \xi^\alpha(z)\xi^\beta(z')e^{-q|z-z'|}\xi^\beta(z')\xi^\alpha(z). \quad (5)$$

For the confinement functions, we assume eigenfunctions of the infinitely deep potential well with two nodes due to the mostly d-like character of electronic orbitals.

To describe light-matter interaction, we assume a circularly polarized electric field selecting dipoles in the K-valley between like-spin bands. The numerical values for the intra-layer dipoles are computed using the simple lattice model from ref. 36, where we neglect the momentum dependence. For the inter-layer transition dipoles, we assume a value that is 10 times smaller than that in the $MoSe_2$ monolayer [28].

The SBE contains a phenomenological damping factor γ, which corresponds to the HWHM of lines in optical spectra. Due to excitation-induced dephasing, γ depends on the actual excited-carrier density. We fix the value of γ at different densities by matching simulated and experimental reflectance spectra. For the intra-layer $MoSe_2$ transition, this yields γ=25 meV for carrier density n = 1.3x10^{12} cm^{-2}, γ = 30 meV for n = 1.9x10^{12} cm^{-2}, γ = 35 meV for n = 5.3x10^{12} cm^{-2} and γ = 50 meV for n = 3.13x10^{13} cm^{-2} . For the intra-layer WSe_2 transition, we use a γ that is 50% larger to account for the stronger dephasing, in accordance with the experimental reflectance spectra.

Fig. 4a shows simulated transient reflectance spectra at excitation densities $n_0 = 6x10^{11}$, $4x10^{12}$, and $3x10^{13}$ cm^{-2}, obtained from theoretical optical absorptance and the experimental sample geometry. Also shown as comparison are experimental transient reflectance spectra (Δt = 1 ps) at similar n_0 values, Fig. 4b. The simulations and experimental spectra are in excellent agreement,

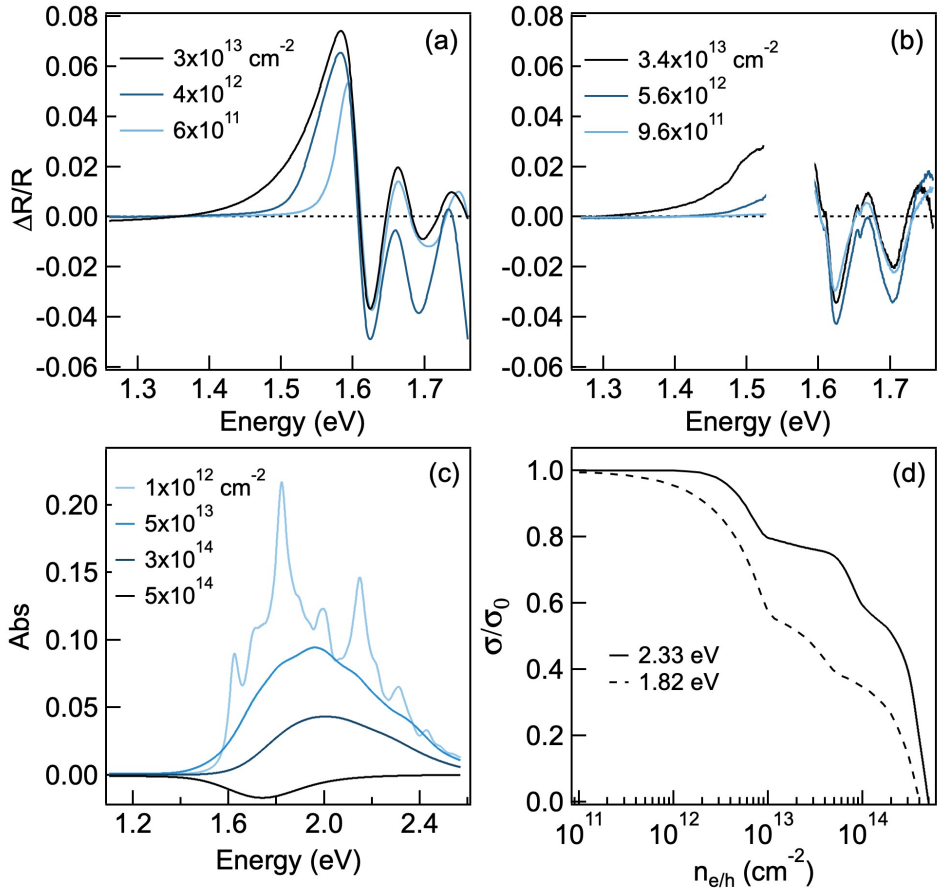

Fig.4. Calculated optical spectra of the WSe2/MoSe2 hetero-bilayer. (a) Simulated reflectance spectra from theoretical optical spectra and experimental sample geometry at the indicated excitation densities ($n_{eh} = 6x10^{11}$- $3x10^{13}$ cm^{-2}); (b) Experimental reflectance spectra at Δt = 1 ps at initial excitation densities of $n_0 = 9.6x10^{11}$-$3.4x10^{13}$ cm^{-2}; (c) Calculated optical absorptance spectra at $n_{eh} = 1x10^{11}$-$5x10^{14}$ cm^{-2}; (d) Calculated relative optical absorptance as a function of n_{eh} at two photon energies used in the experiments.

including main features of bleaching of intralayer excitonic transitions for all excitation densities, the broad induced absorption feature above the Mott density, and stimulated emission near the renormalized bandgap at ~1.3 eV. This agreement provides strong support for the conclusion on

Mott transition from the interlayer exciton to charge separated e/h plasma, as well as for the calibration of carrier density in the CW measurement in Fig. 1.

Fig. 4c show calculated absorptance spectra at selected n_{eh} values. By determining at which n_{eh} excitonic absorption resonance becomes bleached, we find $n_{Mott} = 3\text{x}10^{12}$ cm^{-2}. This value is close to $n_{Mott} = 1.6\text{x}10^{12}$ cm^{-2} obtained from an analytical estimate[29] of $a_0 n_{Mott}^{1/2} \approx 0.25$ and an interlayer exciton radius of ~2 nm [14]. More specifically, we follow excitonic absorption where exciton features gradually fade through broadening from a clear peak to transparency and eventually to gain [24,37]. Below n_{Mott}, the presence of excitons significantly reduces scattering. There is an accelerated broadening after excitons cease to exist above n_{Mott} [24] and this leaves a signature in increased PL linewidth. Note that the observed increase in PL peak width above the Mott density is much larger than what was observed before in coupled III-V quantum wells[11,12]. The inter-layer excitons in the 2D TMDC hetero-bilayer[7–10] is much more strongly bound and less Coulomb screened than their counter parts in III-V coupled quantum wells[11,12]; as a result, the Mott transition has a much larger effect on reducing Coulomb screening in the former.

In addition to revealing the Mott threshold from the disappearance of sharp excitonic features, the theoretical absorption spectra show the decrease in oscillator strength with increasing n_{eh}, as expected from Pauli blocking and screening effects. Optical transparency is reached at $n_{eh} \sim 4\text{x}10^{14}$ cm^{-2} above which stimulated emission dominates. Based on the calculated optical spectra, we obtain the n_{eh}-dependent relative absorptance (σ/σ_0, where σ_0 is the absorptance at the low n_{eh} limit) shown in Fig. 4d for two photon energies. These calculated results are used in the calibration of experimental excitation densities (see Supporting Materials, Fig. S7).

Mechanisms of Interlayer PL Emission from the Hetero-bilayer

We now turn to the mechanism of PL emission from interlayer excitons and charge separated e/h plasmas. A comparison of TRPL in Fig. 2 and transient reflectance in Fig. 3 reveals a major discrepancy in the time scales involved. PL decays are characterized by time constants of ~10^2 ns, but transient reflectance features time constants in the range of $10^{1\text{-}2}$ ps. We show kinetic profiles (vertical cuts of transient reflectance spectra) for two representative probe energies, hν = 1.351 eV and 1.624 eV for induced absorption (Fig. 3g) and photo-bleaching (Fig. 3h), respectively. Fig. 3g

shows little induced absorption at hν = 1.351 eV, for n_0 = 1x10^{11} cm^{-2} and 9.6x10^{11} cm^{-2}, as expected from the absence of plasmas. When n_0 is increased above n_{Mott}, we observe both positive (induced absorption) and negative (stimulated emission) $\Delta R/R_0$ signal, consistent with the transformation to the charge separated plasma region. For the intermediate density n_0 = 5.6x10^{12} cm^{-2}, stimulated emission dominates. At the highest density of n_0 = 3.4x10^{13} cm^{-2}, induced absorption dominates at $\Delta t < 60$ ps and stimulated emission at $\Delta t > 60$ ps.

The kinetics profiles at hν = 1.624 eV, Fig. 3h, reveal the short time nature of photo-bleaching. At n_0 = 1x10^{11}, 9.6x10^{11}, and 5.6x10^{12} cm^{-2}, photo-bleaching ($-\Delta R/R_0$) grows with time constants of τ_1 = 140±30 fs, attributed to the ultrafast dissociation of intralayer excitons in each TMDC monolayer to form charge separated states that increase the Pauli blocking effect. The photo-bleaching intensity peaks in sub-picoseconds and decays on longer time scales. At $n_0 \leq n_{Mott}$ (1x10^{11} cm^{-2} and 9.6x10^{11} cm^{-2}), bleaching intensity decays with time constants of τ_2 = 30±10 ps. This time constant increases above n_{Mott} to τ_2 = 90±30 ps and τ_2 = 290±60 ps at n_0 = 5.6x10^{12} cm^{-2} and 3.4x10^{13} cm^{-2}, respectively. There is a three-order of magnitude difference between the time constants for PL decay (τ_{PL}) and those of photo-bleaching recovery (τ_2). The fast recovery in photo-bleaching cannot result from the loss of photo-excited charge carriers to recombination, but rather to the scattering of these carriers away from the K valley. Computational studies on the $WSe_2/MoSe_2$ hetero-bilayer have shown that the conduction band is lower in energy at the Q point than that at the K point, while valence band energy at the Γ point is close in energy to that of the K point [14]. Following charge separation, inter-valley scattering transfers carrier populations in the K valleys to the Q and Γ valleys. This process reduces Pauli blocking of optical transitions in the K valleys and accounts for the τ_2 = 30-290 ps decay time constants. Efficient intervalley carrier scattering involves optical phonons and its rate is decreased by screening as excitation density is increased, thus accounting for longer τ_2 at higher n_0 above n_{Mott}. The Q and Γ valleys serve as carrier reservoirs; the momentum-indirect nature prohibits radiative recombination of electrons and holes in these valleys. Instead, scattering of electrons and holes back to the K valleys likely occurs before radiative recombination happens. This explains the long PL lifetimes on the 10^2 ns timescale. In a similar proposal, dark traps have been suggested as exciton reservoirs for slow PL emission in monolayer MoS_2 [38].

DISCUSSION

The results presented here establish photo-induced charge separation at van der Waals interfaces as an effective means to control 2D charge carrier densities. Using the hetero-bilayer of $WSe_2/MoSe_2$, we show spectroscopic signature of Mott transition from interlayer excitons to charge separated electron/hole plasmas, in excellent agreement with calculation based on a fully microscopic quantum theory. We point out that the spectroscopy measurements probe the combined responses of the electron plasma and hole plasma across the hetero-bilayer interface. Resolving the individual response of the electron or hole plasma is challenging, but possible with time-resolved and angle-resolved photoemission spectroscopy (tr-ARPES), which is underway in our laboratory[39]. The combined photoluminescence and transient reflectance measurements also reveal the participation of intervalley scattering and dark exciton/carrier reservoirs in radiative recombination dynamics. Remarkable, photo-induced charge separation under CW conditions allows us to reach charge carrier densities as high as ~$4x10^{14}$ cm^{-2}, which is two orders of magnitude above the Mott density and is at the same level demonstrated previously for gate-doped superconductivity in TMDCs [1–4]. These findings suggest that photo-induced charge separation at van der Waals interfaces is an effective means to realize complex electronic phases in 2D materials, particularly photo-induced superconductivity under CW conditions.

MATERIALS and METHODS

Preparation of 2D $WSe_2/MoSe_2$ hetero-bilayer samples

Monolayers of WSe_2 and $MoSe_2$ were mechanically exfoliated from bulk crystals grown by the self-flux method. These monolayers possessed low defect densities (<10^{11} cm^{-2}) [16]. Hexagonal boron nitride (h-BN) flakes of thickness 5 – 35 nm and of flat surfaces were also obtained by mechanical exfoliation. The flakes (WSe_2, $MoSe_2$, and BN) were characterized by atomic force microscopy (AFM) and Raman spectroscopy.

The crystal orientations of WSe_2 and $MoSe_2$ monolayers were determined by second harmonic generation (SHG) measurement on an inverted optical microscope (Olympus IX73). Linearly polarized femtosecond laser light (Coherent Mira 900, 80 MHz, 800 nm, 100 fs) was focused onto a monolayer with a 100x, NA 0.80 objective (Olympus LMPLFLN100X). The reflected SHG

signal at 400 nm was collected by the same objective, filtered by a short-pass dichroic mirror, short-pass and band-pass filters, and a Glan-Taylor linear polarizer, detected by a photomultiplier tube (Hamamatsu R4220P), and recorded by a photon counter (Stanford Research Systems SR400). We obtain the azimuthal angular (θ) distribution of SHG signal by rotating either the sample [40] or the laser polarization [41] (via a half waveplate) with fixed-polarization detection. Due to the D_{3h} symmetry, the non-vanishing tensor elements of the second order susceptibility of WSe_2 and $MoSe_2$ monolayers are $\chi^{(2)}_{yyy} = -\chi^{(2)}_{yxx} = -\chi^{(2)}_{xxy} = -\chi^{(2)}_{xyx}$ where the *x* axis is defined as the zigzag direction (*1*). When we rotated the sample, the SHG intensity showed six-fold symmetry: $I_{\perp} \propto cos^2(3\theta)$ and $I_{\parallel} \propto sin^2(3\theta)$, where θ is the angle between the laser polarization and the zigzag direction. When we rotate the laser polarization, the SHG intensity showed four fold symmetry: $I_y \propto cos^2(2\theta)$ and $I_x \propto sin^2(2\theta)$. We use triangular flakes of monolayer WS_2 (6Carbon) or MoS_2 (2DLayer), where zigzag directions are the same as crystal edges, both grown from chemical vapor deposition (CVD), to calibrate the SHG setup.

The 2D $WSe_2/MoSe_2$ hetero-bilayer was prepared by the polymer-free van der Waals assembly technique [42]. A transparent polydimethylsiloxane (PDMS) stamp coated by a thin layer of polypropylene carbonate (PPC) was used to pick up a thin layer of exfoliated h-BN. This h-BN was then used to pick up the first TMDC monolayer. The second TMDC monolayer was aligned to and picked up by the first monolayer on a high precision rotation stage. The heterostructure was finally stamped onto a thicker layer of h-BN and detached from PPC at elevated temperatures (90-120 °C). The residual PPC was washed away by acetone to give a clean h-BN/$MoSe_2$/WSe_2/h-BN heterostructure on the Si/SiO2 substrate.

Fig. S1 shows optical microscope images of the two BN/WSe_2/$MoSe_2$/BN hetero-bilayer samples used in the spectroscopy measurements shown in the main text. Fig. S2 and S3 show SHG polarization data used to determine the two alignment angles, θ = 4±2° and 13±2°, respectively.

Steady-state and time-resolved photoluminescence measurements

All spectroscopic measurements were performed on a home-built reflection microscope system based on a liquid-helium recirculating optical cryostat (Montana Instruments Fusion/X-Plane) with a 100x, NA 0.75 objective (Zeiss LD EC Epiplan-Neofluar 100x/0.75 HD DIC M27). The

temperature of the sample stage could be varied between 3 K and 350 K. In all experiments presented in this study, the TMDC hetero-bilayer and monolayers samples were at 4 K in a vacuum ($<10^{-6}$ torr) environment, unless otherwise noted.

In steady-state photoluminescence (PL) measurements, continuous wave (CW) laser (532 nm) was focused by the objective to a diffraction limited spot on the sample. The excitation power was measured by a calibrated power meter (Ophir StarLite) with broad dynamic range. The PL light was collected by the same objective, spectrally filtered, dispersed by a grating and detected by an InGaAs photodiode array (Princeton Instruments PyLoN-IR). The wavelength was calibrated by neon-argon and mercury atomic emission sources (Princeton Instruments IntelliCal). The intensity was calibrated by three independent NIST traceable light sources: a 400 - 1050 nm tungsten halogen lamp (StellarNet SL1-CAL), a 250 - 2400 nm quartz tungsten halogen lamp (Oriel 63355) and a 425 - 1000 nm LED (Princeton Instruments IntelliCal).

In time-resolved photoluminescence (TRPL) measurements, the pulsed excitation light ($h\nu$ = (1.82 eV, pulse duration 150 fs) was from a wavelength tunable output of an visible optical parametric amplifier (Coherent OPA 9450) pumped by a Ti:Sapphire regenerative amplifier (Coherent RegA 9050, 250 kHz, 800 nm, 100 fs). The interlayer PL emission in the 900 – 1000 nm region was selected and focused onto a single photon avalanche photodiode (IDQ ID100-50). The TRPL trace was collected with a time-correlated single photon counting module (bh SPC-130). The instrument response function, determined by collecting scattered laser light, has a full-width-at-half-maximum (FWHM) of 100 ps, Fig. S5. The time resolution of TRPL was estimated at ~20% of the FWHM, i.e. ~20 ps.

Reflectance and transient reflectance measurements

In reflectance measurements, the broadband white light was directed to the sample with the objective, reflected, collected by the same objective, and detected by an InGaAs photodiode array (Princeton Instruments PyLoN-IR). For the reflectance at the low density limit, the spectrally filtered and collimated white light from a 3200 K halogen lamp (KLS EKE/AL) was used. Reflectance was also taken for the white light probe in the same geometry as transient reflectance to confirm that it is in the linear regime. A 150 nm gold film deposited by e-beam evaporation on the same Si/SiO_2 substrate was used as a reflectance standard.

In transient reflectance measurements, femtosecond laser pulses from the Ti:Sapphire regenerative amplifier (Coherent RegA 9050, 250 kHz, 800 nm, 100 fs) was split into two beams: one was used to pump the visible optical parametric amplifier (Coherent OPA 9450) to generate tunable pump light and the other was focused onto a sapphire crystal to generate white light continuum probe light. The pump was then chirp compensated by a prism pair, delayed by a motorized translation stage, modulated by an optical chopper, combined with the probe and directed collinearly to the sample by the objective. In order to achieve homogenous excitation, average over a sufficient area and reduce nonlinear effect of probe, both beams were focused onto the back focal plane of the objective to obtain a large beam diameter at the sample plane, unless otherwise specified. The reflected probe light was then collected by the same objective, spectrally filtered to remove pump light and recorded with the InGaAs photodiode array (Princeton Instruments PyLoN-IR). This detector was synchronized with the optical chopper through a home-made frequency doubler. At each specific pump-probe delay, the reflected probe spectra with and without pump was recorded and the transient reflectance ($\Delta R/R$) was calculated. We determined the sign of the transient reflectance signal by recording the chopper output with a data acquisition (DAQ) board (National Instruments) triggered by the InGaAs detector. The chopper modulation frequency was selected to maximize the signal-to-noise ratio of transient reflectance signal.

Acknowledgement. The transient reflectance and CW-PL measurements were supported by the National Science Foundation (NSF) grant DMR-1608437 (to XYZ and JH). The TRPL measurements were supported by NSF grant DMR-1809680 (to XYZ). Sample preparation, purchase of the recirculating He-cryostat, and optical setup were supported by the Center for Precision Assembly of Superstratic and Superatomic Solids, a Materials Science and Engineering Research Center (MRSEC) through NSF grant DMR-1420643. The control experiments on charge separation in the misaligned heterojunction (Fig. S10) were supported by Office of Naval Research under award no. N00014-16-1-2921. AS, MF, and F.J. acknowledge support for the theoretical calculation from the Deutsche Forschungsgemeinschaft (RTG 2247 Quantum Mechanical Materials Modelling) and resources for computational time at the HLRN (Hannover/Berlin).

Author contributions. XYZ and JH conceived this work. JW, JA, and YB performed the experiments. AS and MF carried out the theoretical calculations, with supervision from ML and

FJ. XX participated in the interpretation of experimental findings. XYZ, MK, and JH wrote the manuscript, with inputs from all coauthors. All authors read and commented on the manuscript.

Data Availability. All data needed to evaluate the conclusions in the paper are present in the paper and/or the Supplementary Materials. Additional data related to this paper may be requested from the authors.

Competing Interests. All authors declare that they have no competing interests.

References

1. Li, L. J. *et al.* Controlling many-body states by the electric-field effect in a two-dimensional material. *Nature* **529,** 185–189 (2016).
2. Saito, Y. *et al.* Superconductivity protected by spin–valley locking in ion-gated MoS2. *Nat. Phys.* **12,** 144–149 (2015).
3. Lu, J. M. *et al.* Evidence for two-dimensional Ising superconductivity in gated MoS2. *Science* **350,** 1353–1357 (2015).
4. Lu, J. M. *et al.* Full superconducting dome of strong Ising protection in gated monolayer WS2. *Proc. Natl. Acad. Sci. U. S. A.* **115,** 3551–3556 (2018).
5. Hong, X. *et al.* Ultrafast charge transfer in atomically thin MoS2/WS2 heterostructures. *Nat. Nanotechnol.* **9,** 682 (2014).
6. Zhu, H. *et al.* Interfacial Charge Transfer Circumventing Momentum Mismatch at Two-Dimensional van der Waals Heterojunctions. *Nano Lett.* **17,** 3591–3598 (2017).
7. Rivera, P. *et al.* Observation of long-lived interlayer excitons in monolayer MoSe2–WSe2 heterostructures. *Nat. Commun.* **6,** 6242 (2015).
8. Kunstmann, J. *et al.* Momentum-space indirect interlayer excitons in transition-metal dichalcogenide van der Waals heterostructures. *Nat. Phys.* **14,** 801–805 (2018).
9. Kim, J. *et al.* Observation of ultralong valley lifetime in WSe2/MoS2 heterostructures. *Sci. Adv.* **3,** e1700518 (2017).
10. Rivera, P. *et al.* Interlayer valley excitons in heterobilayers of transition metal dichalcogenides. *Nat. Nanotechnol.* **13,** 1004–1015 (2018).
11. Stern, M., Garmider, V., Umansky, V. & Bar-Joseph, I. Mott transition of excitons in coupled quantum wells. *Phys. Rev. Lett.* **100,** 256402 (2008).
12. Kiršanskė, G. *et al.* Observation of the exciton Mott transition in the photoluminescence of coupled quantum wells. *Phys. Rev. B* **94,** 155438 (2016).
13. Chernikov, A., Ruppert, C., Hill, H. M., Rigosi, A. F. & Heinz, T. F. Population inversion and giant bandgap renormalization in atomically thin WS2 layers. *Nat. Photonics* **9,** 466–469 (2015).
14. Gillen, R. & Maultzsch, J. Interlayer excitons in MoSe2/WSe2 heterostructures from first principles. *Phys. Rev. B* **97,** 165306 (2018).
15. Yu, H., Wang, Y., Tong, Q., Xu, X. & Yao, W. Anomalous light cones and valley optical selection rules of interlayer excitons in twisted heterobilayers. *Phys Rev Lett* **115,** 187002 (2015).

16. Edelberg, D. *et al.* Hundredfold Enhancement of Light Emission via Defect Control in Monolayer Transition-Metal Dichalcogenides. *arXiv Prepr. arXiv1805.00127* (2018).

17. Li, Y. *et al.* Measurement of the optical dielectric function of monolayer transition-metal dichalcogenides: MoS2, MoSe2, WS2, and WSe2. *Phys. Rev. B* **90,** 205422 (2014).

18. Ross, J. S. *et al.* Electrical control of neutral and charged excitons in a monolayer semiconductor. *Nat. Commun.* **4,** 1474 (2013).

19. Ye, Z. *et al.* Efficient generation of neutral and charged biexcitons in encapsulated WSe 2 monolayers. *Nat. Commun.* **9,** 3718 (2018).

20. Barbone, M. *et al.* Charge-tuneable biexciton complexes in monolayer WSe2. *Nat. Commun.* **9,** 3721 (2018).

21. Chen, S.-Y., Goldstein, T., Taniguchi, T., Watanabe, K. & Yan, J. Coulomb-bound four- and five-particle intervalley states in an atomically-thin semiconductor. *Nat. Commun.* **9,** 3717 (2018).

22. Rivera, P. *et al.* Valley-polarized exciton dynamics in a 2D semiconductor heterostructure. *Science* **351,** 688–691 (2016).

23. Stern, M., Umansky, V. & Bar-Joseph, I. Exciton Liquid in Coupled Quantum Wells. *Science* **343,** 55–57 (2014).

24. Smith, R. P. *et al.* Extraction of many-body configurations from nonlinear absorption in semiconductor quantum wells. *Phys. Rev. Lett.* **104,** 247401 (2010).

25. Chatterjee, S. *et al.* Excitonic photoluminescence in semiconductor quantum wells: plasma versus excitons. *Phys. Rev. Lett.* **92,** 67402 (2004).

26. Miller, B. *et al.* Long-Lived Direct and Indirect Interlayer Excitons in van der Waals Heterostructures. *Nano Lett.* **17,** 5229–5237 (2017).

27. Mak, K. F. *et al.* Measurement of the optical conductivity of graphene. *Phys. Rev. Lett.* **101,** 196405 (2008).

28. Ross, J. S. *et al.* Interlayer Exciton Optoelectronics in a 2D Heterostructure p-n Junction. *Nano Lett.* **17,** 638–643 (2017).

29. Meckbach, L., Stroucken, T. & Koch, S. W. Giant excitation induced bandgap renormalization in TMDC monolayers. *Appl. Phys. Lett.* **112,** 061104 (2018).

30. Haug, H. & Koch, S. W. *Quantum Theory of the Optical and Electronic Properties of Semiconductors*. (WORLD SCIENTIFIC, 2009). doi:10.1142/7184

31. Steinhoff, A., Rosner, M., Jahnke, F., Wehling, T. O. & Gies, C. Influence of excited carriers on the optical and electronic properties of MoS2. *Nano Lett.* **14,** 3743–3748 (2014).

32. Kormányos, A; Burkard, G.; Gmitra, M.; Fabian, J; Zólyomi, V.; Drummond, ND; Fal'ko, V. k·p theory for two-dimensional transition metal dichalcogenide semiconductors. *2D Mater.* **2,** 22001 (2015).

33. Florian, M. *et al.* The dielectric impact of layer distances on exciton and trion binding energies in van der Waals heterostructures. *Nano Lett.* **18,** 2725–2732 (2018).

34. Kylänpää, I. & Komsa, H.-P. Binding energies of exciton complexes in transition metal dichalcogenide monolayers and effect of dielectric environment. *Phys. Rev. B* **92,** 205418 (2015).

35. Geick, R., Perry, C. H. & Rupprecht, G. Normal modes in hexagonal boron nitride. *Phys. Rev.* **146,** 543 (1966).

36. Xiao, D., Liu, G. Bin, Feng, W., Xu, X. & Yao, W. Coupled spin and valley physics in monolayers of MoS 2 and other group-VI dichalcogenides. *Phys. Rev. Lett.* **108,** 196802 (2012).

37. Sie, E. J. *et al.* Observation of Exciton Redshift-Blueshift Crossover in Monolayer WS2. *Nano Lett.* **17,** 4210–4216 (2017).

38. Goodman, A. J., Willard, A. P. & Tisdale, W. A. Exciton trapping is responsible for the long apparent lifetime in acid-treated MoS2. *Phys. Rev. B* **96,** 121404 (2017).

39. Liu, F., Ziffer, M., Hansen, K. R., Wang, J. & Zhu, X. -Y. Direct Determination of Band Gap Renormalization in Photo-Excited Monolayer MoS2. *Phys. Rev. Lett.* (2019) in press.

40. Li, Y. *et al.* Probing symmetry properties of few-layer MoS2 and h-BN by optical second-harmonic generation. *Nano Lett.* **13,** 3329–3333 (2013).

41. Mannebach, E. & Duerloo, K. Ultrafast Electronic and Structural Response of Monolayer MoS2 under Intense Photoexcitation Conditions. *Acs …* (2014). at <http://pubs.acs.org/doi/abs/10.1021/nn5044542>

42. Wang, L. *et al.* One-dimensional electrical contact to a two-dimensional material. *Science* **342,** 614–7 (2013).

43. Laturia, A., Van de Put, M. L. & Vandenberghe, W. G. Dielectric properties of hexagonal boron nitride and transition metal dichalcogenides: from monolayer to bulk. *npj 2D Mater. Appl.* **2,** 6 (2018).

44. Kira, M., Jahnke, F., Hoyer, W. & Koch, S. W. Quantum theory of spontaneous emission and coherent effects in semiconductor microstructures. *Prog. quantum Electron.* **23,** 189–279 (1999).

45. Aspnes, D. E. & Theeten, J. B. Spectroscopic analysis of the interface between Si and its thermally grown oxide. *J. Electrochem. Soc.* **127,** 1359–1365 (1980).

46. Malitson, I. H. Interspecimen comparison of the refractive index of fused silica. *JOSA* **55,** 1205–1209 (1965).

47. Segura, A. *et al.* Natural optical anisotropy of h-BN: Highest giant birefringence in a bulk crystal through the mid-infrared to ultraviolet range. *Phys. Rev. Mater.* **2,** 24001 (2018).

48. Wang, G. *et al.* Giant enhancement of the optical second-harmonic emission of WSe 2 monolayers by laser excitation at exciton resonances. *Phys. Rev. Lett.* **114,** 97403 (2015).

49. Wang, G. *et al.* Exciton states in monolayer MoSe2: impact on interband transitions. *2D Mater.* **2,** 45005 (2015).